mater.scichina.com link.springer.com

Published online 25 May 2022 | https://doi.org/10.1007/s40843-022-2061-x
Sci China Mater 2022, 65(10): 2685–2693

Stoichiometry design in hierarchical CoNiFe phosphide for highly efficient water oxidation

Jiangbo Chen[1], Jie Ying[2*], Yuxuan Xiao[2], Yuan Dong[1], Kenneth I. Ozoemena[3], Silvia Lenaerts[4] and Xiaoyu Yang[1,5*]

ABSTRACT **Rational composition design of trimetallic phosphide catalysts is of significant importance for enhanced surface reaction and efficient catalytic performance. Herein, hierarchical $Co_xNi_yFe_zP$ with precise control of stoichiometric metallic elements (x:y:z = (1–10):(1–10):1) has been synthesized, and $Co_{1.3}Ni_{0.5}Fe_{0.2}P$, as the most optimal composition, exhibits remarkable catalytic activity (η = 320 mV at 10 mA cm^{-2}) and long-term stability (ignorable decrease after 10 h continuous test at the current density of 10 mA cm^{-2}) toward oxygen evolution reaction (OER). It is found that the surface P in $Co_{1.3}Ni_{0.5}Fe_{0.2}P$ was replaced by O under the OER process. The density function theory calculations before and after long-term stability tests suggest the clear increasing of the density of states near the Fermi level of $Co_{1.3}Ni_{0.5}Fe_{0.2}P$/$Co_{1.3}Ni_{0.5}Fe_{0.2}O$, which could enhance the OH$^-$ adsorption of our electrocatalysts and the corresponding OER performance.**

Keywords: trimetallic phosphides, hierarchical structures, stoichiometry design, charge transfer, oxygen evolution reaction

INTRODUCTION

Transition metal phosphides are emerging for the design of electrocatalysts, and multi-metallic phosphides are of more interest for significant enhancement of electrocatalytic activity [1,2]. Generally, integrating multiple metallic elements into a single nano-architecture offers a common promise of material properties that could exceed a single element [3–7]. The current approaches to the multi-metallic phosphides mainly arise from wet-chemistry synthesis, through which a variety of binary metallic phosphides with adjusting stoichiometric compositions can be attained [8–11]. However, there are rare reports on exceeding two metallic elements and stoichiometric adjustment, because the different hydrolysis and condensation rates of any two more independent precursors would not lead to the formation of homogeneous phase and precise control of stoichiometric elements [4,12].

From the view of electrocatalysis such as oxygen evolution reaction (OER), many issues of transition metal phosphides need to be addressed. Firstly, moderate chemisorption thermodynamics is preferred, OH$^-$ needs fast adsorption, but the bonding interactions of M–O in the intermediates (MOH, MO, and MOOH) should not be too strong, as this might hinder the fast desorption of oxygen [13]. Next, fast electron transfer between the reactants/intermediates and the catalytic active center is also favorable [14]. Finally, the optimization of the M–P binding energy shifts could modulate the electronic structure and greatly improve their catalytic properties [12,15]. Note that stoichiometric adjustment of multiple metals provides a possibility of the simplest high-performance design of transition metal phosphides. As an example, the oxophilicity of the catalysts in OER could depend on composition adjustment of the nanoalloys for the adsorption of intermediates, and the proper ad/desorption [16].

Cobalt (Co), nickel (Ni), and iron (Fe), as the most common metals for transition metal phosphides, have shown great potential in the design of high-performance OER catalysts [12,17,18]. There are many successful examples of composition adjustment for enhancing OER activities. Ni-doped CoP can effectively adjust the binding energy of intermediates to the optimal value, thus improving the thermodynamics toward OER [4]. A few Fe-doping in CoP can promote the fracture of Co–O bond and the formation of O–O bond and enhance their OER performance [19]. Subsequently, ternary metal phosphide by doping CoP with Ni and Fe has been proven to improve the local electrostatic interaction between metal cations and OH$^-$ groups and OER kinetics [12]. However, only 1:1:1 metal ratio of CoNiFeP is obtained, and the ratio of Co/Ni/Fe is not easy to be precisely adjusted during the uncontrolled oxidation reaction and complex cooperation structure involving ionic reactions in liquid phase environments because of the difference in reduction potential of Co^{2+} (−0.282 V), Ni^{2+} (−0.236 V) and Fe^{2+} (−0.440 V) (Note S1) [12,18]. Therefore, the effective control of the stoichiometric ratio of ternary metals is still a major challenge.

A simple phosphating approach is phosphorization of the metallic hydroxides, which avoids the above-mentioned uncontrolled oxidation and complex cooperation [3,20,21]. For

[1] State Key Laboratory of Advanced Technology for Materials Synthesis and Processing, School of Materials Science and Engineering & Shenzhen Research Institute & Joint Laboratory for Marine Advanced Materials in Pilot National Laboratory for Marine Science and Technology (Qingdao), Wuhan University of Technology, Wuhan 430070, China
[2] School of Chemical Engineering and Technology, Sun Yat-sen University, Zhuhai 519082, China
[3] Molecular Sciences Institute, School of Chemistry, University of the Witwatersrand, Private Bag 3, Johannesburg 2050, South Africa
[4] Research Group Sustainable Energy, Air and Water Technology, Department of Bioscience Engineering, University of Antwerp, Antwerp 2020, Belgium
[5] School of Engineering and Applied Sciences, Harvard University, Cambridge, Massachusetts 02138, USA
* Corresponding authors (emails: yingj5@mail.sysu.edu.cn (Ying J); xyyang@seas.harvard.edu or xyyang@whut.edu.cn (Yang XY))

Co, Ni, and Fe, their ions with two valences not only show similar solubility product constants (K_{sp} of $Co(OH)_2 \approx 1.6 \times 10^{-15}$, K_{sp} of $Ni(OH)_2 \approx 2.0 \times 10^{-15}$, and K_{sp} of $Fe(OH)_2 \approx 1.0 \times 10^{-15}$; Table S1) for possible stoichiometry adjustment by the full precipitation of initial precursors, but also have very similar ion radii (r of $Co^{2+} \approx 0.065$ nm, r of $Ni^{2+} \approx 0.069$ nm and r of $Fe^{2+} \approx 0.061$ nm; Table S1) for homogenous distribution [9,22,23]. Considering that the precipitation rate is often too fast to precisely control, a controllable release of OH^- is used to form the ternary metal phosphides with stoichiometry control and homogenous composition. Herein, hierarchical $Co_xNi_yFe_zP$ with precise control of stoichiometric metallic elements (x:y:z = (1–10):(1–10):1) has been synthesized by controllable full-precipitation and co-phosphorization of Co-Ni-Fe hydroxides with two valences. The resulting hierarchical $Co_{1.3}Ni_{0.5}Fe_{0.2}P$ shows the most optimal composition and excellent electrocatalytic activity and stability for OER in the alkaline electrolyte, displaying a small overpotential of only 320 mV at the current density of 10 mA cm^{-2}, a dramatically reduced Tafel slope of 45 mV dec^{-1}, as well as a negligible increment after 10 h at the current density of 10 mA cm^{-2} in the chronopotentiometric measurement. Surface reconstruction from metal phosphides into metal oxides has been found in hierarchical $Co_{1.3}Ni_{0.5}Fe_{0.2}P$ in the OER process. The theoretical calculations suggest that the adsorption of OH^- on $Co_{1.3}Ni_{0.5}Fe_{0.2}P/Co_{1.3}Ni_{0.5}Fe_{0.2}O$ surface is more thermoneutral than those of $Co_{0.7}Ni_{0.7}Fe_{0.7}P/Co_{0.7}Ni_{0.7}Fe_{0.7}O$, $Co_{1.4}Ni_{0.6}P/Co_{1.4}Ni_{0.6}O$, and Co_2P/Co_2O, which is beneficial for OER performance enhancement.

RESULTS AND DISCUSSION

Formation mechanism and electrochemical tests

The overall synthetic route for hierarchical $Co_xNi_yFe_zP$ includes three steps (Fig. 1). Cu_2O octahedrons around 1.5 μm in size (Fig. S1a, b) were first synthesized as the template of controllable release of OH^-. Then, Co^{2+}, Ni^{2+}, and Fe^{2+} species with various molar ratios were added to synthesize the hydroxides of $Co_xNi_yFe_z$ in the presence of $Na_2S_2O_3$, which functioned to coordinate and etch Cu_2O through forming a soluble complex [24] $[Cu_2(S_2O_3)_x]^{2-2x}$ ($Cu_2O + xS_2O_3^{2-} + H_2O \rightarrow [Cu_2(S_2O_3)_x]^{2-2x} + OH^-$). The controlled released OH^- reacted with Co^{2+}, Ni^{2+}, and Fe^{2+} species to generate insoluble CoNiFe hydroxides. These hydroxides of $Co_xNi_yFe_z$ can have an adjustable ratio of the metals. Finally, $Co_xNi_yFe_z(OH)_2$ products were completely converted into $Co_xNi_yFe_zP$ by a simple phosphorization reaction (Note S2).

To prove the precise control of the ratio of Co/Ni/Fe, the $Co^{2+}/Ni^{2+}/Fe^{2+}$ precursors with different molar ratios (1.6Co/0.2Ni/0.2Fe, 1.3Co/0.5Ni/0.2Fe, 0.9Co/0.9Ni/0.2Fe, 0.5Co/1.3Ni/0.2Fe, 0.7Co/0.7Ni/0.7Fe, 1.0Co/0.5N/0.5Fe, 1.3Co/0.3Ni/0.3Fe, 1.0Co/1.0Ni/0.1Fe) were used to synthesize the corresponding $Co_xNi_yFe_zP$. Surprisingly, as shown in Table S2, the final ratios of $Co_xNi_yFe_zP$ were in very good agreement with the initial precursor ratios. $Co_{1.6}Ni_{0.2}Fe_{0.2}P$, $Co_{1.3}Ni_{0.5}Fe_{0.2}P$, $Co_{0.9}Ni_{0.9}Fe_{0.2}P$, $Co_{0.5}Ni_{1.3}Fe_{0.2}P$, $Co_{0.7}Ni_{0.7}Fe_{0.7}P$, $Co_{1.0}Ni_{0.5}Fe_{0.5}P$, $Co_{1.3}Ni_{0.3}Fe_{0.3}P$, and $Co_{1.0}Ni_{1.0}Fe_{0.1}P$ were obtained and their compositions were verified by the inductively coupled plasma-atomic emission spectrometry (ICP-AES). As a comparison, the binary $Co_{1.8}Fe_{0.2}P$, $Co_{1.4}Ni_{0.6}P$ and $Ni_{1.5}Fe_{0.5}P$ were also obtained by the adjustment of initial ratios of CoFe, CoNi, and NiFe precursors (Table S2). Notably, the metal ions with two valences were critical for precise control. For example, when the Fe^{2+} was substituted by Fe^{3+} with different solubility product constants (K_{sp} of $Fe(OH)_3 \approx 3.2 \times 10^{-38}$) and ion radii ($r$ of $Fe^{3+} \approx 0.049$ nm) (Table S1), the resulting CoNiFe trimetallic phosphide showed the similar hierarchical morphology (Fig. S2), but displayed a very big difference in the final molar ratio of Co/Ni/Fe. The final ratio of Co/Ni/Fe is 3.42:1.31:0.20 compared with an initial ratio 1.3:0.5:0.2 of $Co^{2+}/Ni^{2+}/Fe^{3+}$ (Table S2), which means that the metal ions with two valences (Co^{2+} and Ni^{2+}) were in accordance with the rule of precise control, but the metal ion with three valences (Fe^{3+}) was uncontrollable.

The electrocatalytic activity toward OER of the transition metal phosphides including $Co_{1.6}Ni_{0.2}Fe_{0.2}P$, $Co_{1.3}Ni_{0.5}Fe_{0.2}P$, $Co_{0.9}Ni_{0.9}Fe_{0.2}P$, $Co_{0.5}Ni_{1.3}Fe_{0.2}P$, $Co_{0.7}Ni_{0.7}Fe_{0.7}P$, $Co_{1.0}Ni_{0.5}Fe_{0.5}P$, $Co_{1.3}Ni_{0.3}Fe_{0.3}P$, and $Co_{1.0}Ni_{1.0}Fe_{0.1}P$, $Co_{1.4}Ni_{0.6}P$, $Co_{1.8}Fe_{0.2}P$, $Ni_{1.5}Fe_{0.5}P$, Co_2P, Ni_2P were investigated using a standard three-electrode system in a 1.0 mol L^{-1} KOH solution. All these samples showed hierarchical structures with different conformal morphologies as shown in Figs S1c and S3. A slow scan rate of

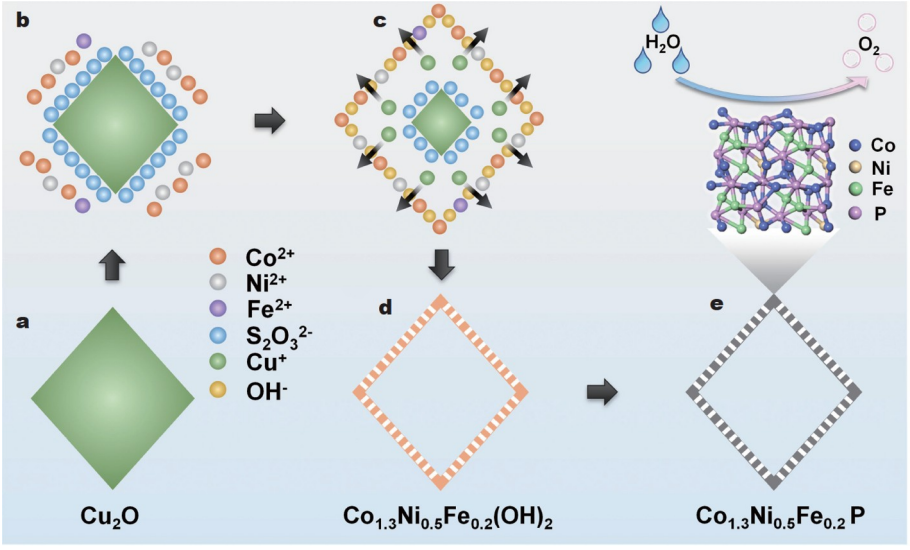

Figure 1 Schematic illustration of the fabrication process of hierarchical $Co_{1.3}Ni_{0.5}Fe_{0.2}P$.

5 mV s^{-1} was used to get linear sweep voltammetry (LSV) curves in order to minimize the capacitive current. Fig. 2a shows the polarization curves (*j*-*V*) obtained by the LSV. It is clearly seen that $Co_{1.3}Ni_{0.5}Fe_{0.2}P$ shows the highest current density at the same overpotentials for OER. To obtain a current density of 10 mA cm^{-2}, $Co_{1.3}Ni_{0.5}Fe_{0.2}P$ represents the lowest overpotential of 320 mV, which is also much lower than that of commercial RuO_2 (376 mV) and other unary and binary metal phosphides including $Co_{1.8}Fe_{0.2}P$ (340 mV), $Co_{1.4}Ni_{0.6}P$ (388 mV), $Ni_{1.5}Fe_{0.5}P$ (447 mV), Co_2P (400 mV), and Ni_2P (483 mV) (Fig. 2b). Notably, the overpotential of $Co_{1.3}Ni_{0.5}Fe_{0.2}P$ is among the best performing transition metal phosphide catalysts in the previous reports (Table S3). It has been shown that Ni could facilitate desorption of OH^- than Co more easily in alkaline solutions, while Co has a higher activity for the Tafel steps than Ni [3,4]. Thus, the surface Ni sites could accelerate water dissociation with high efficiency and the surface Co sites will make it easy for gas generation and release for $Co_xNi_yFe_{0.2}P$ [4,25]. Besides, lattice defects caused by trace iron may provide additional active sites [26].

Appropriate substitution of Ni atoms and/or Fe atoms is closely related to the formation of the perfectly dispersive trimetallic phosphides on the surface. Meanwhile, the OER activity for available surface-active sites can be effectively modulated by optimizing the atomic ratio of Co, Ni, and Fe. On the other hand, $Co_xNi_yFe_zP$ catalysts were also prepared with various Co/Ni/Fe ratios, and it is found that the $Co_{1.3}Ni_{0.5}Fe_{0.2}P$ exhibits an optimal catalytic performance (Fig. S4a, b). This could be explained by the synergistic effect of three elements affecting the surface architectures to expose more active sites and improve the charge transfer between the substitutions and the host metal atom [17]. By means of precisely controlling the Co/Ni/Fe ratio of trimetal phosphides, a much stronger synergistic interplay between three metal centers for promoting the OER performance can be achieved. The Tafel slope plays a non-negligible role in assessing the electrochemical reaction kinetics. A lower Tafel slope value means a faster kinetics [27–29]. The Tafel slope of 45 mV dec^{-1} for $Co_{1.3}Ni_{0.5}Fe_{0.2}P$ is much lower than all other samples' Tafel slopes including all prepared trimetallic phosphides (Fig. S4c) and $Co_{1.8}Fe_{0.2}P$ (56 mV dec^{-1}), RuO_2 (75 mV dec^{-1}), $Co_{1.4}Ni_{0.6}P$ (93 mV dec^{-1}), $Ni_{1.5}Fe_{0.5}P$ (125 mV dec^{-1}), Co_2P (139 mV dec^{-1}), Ni_2P (170 mV dec^{-1}) (Fig. 2c), implying the favorable OER kinetics for $Co_{1.3}Ni_{0.5}Fe_{0.2}P$. Low overpotential, high catalytic current density, and small Tafel slope demonstrate that $Co_{1.3}Ni_{0.5}Fe_{0.2}P$ is highly active.

To further understand the mechanism of enhanced OER performance, electrochemical double-layer capacitance (C_{dl}), which is related to electrochemical active surface area (ECSA), was tested by monitoring the current density in the non-Faradic region with different scan rates (Fig. S5). As shown in Fig. 2d and Fig. S6, it is clear that the C_{dl} of $Co_{1.3}Ni_{0.5}Fe_{0.2}P$ (56.7 mF cm^{-2}) is much larger than that of other control samples such as $Co_{1.8}Fe_{0.2}P$ (45.2 mF cm^{-2}), Co_2P (6.5 mF cm^{-2}), $Co_{1.4}Ni_{0.6}P$ (4.9 mF cm^{-2}), $Ni_{1.5}Fe_{0.5}P$ (0.8 mF cm^{-2}), Ni_2P (0.1 mF cm^{-2}). The large C_{dl} indicates that $Co_{1.3}Ni_{0.5}Fe_{0.2}P$ exposes more active sites, which is supposed to be one of the possible reasons for enhanced OER performance. The charge transfer resistance is related to the electrocatalytic performance of catalysts. The improvement of charge transfer can facilitate the combination of reactants and electrocatalysts and enhance their corresponding performance [13]. Hence, electrochemical impedance spectroscopy (EIS) technique was used to understand the interfacial properties of the electrocatalyst decorated by electrodes (Fig. 2e and Table S4). As expected, the electron-transfer resistance of $Co_{1.3}Ni_{0.5}Fe_{0.2}P$ is much lower than that of

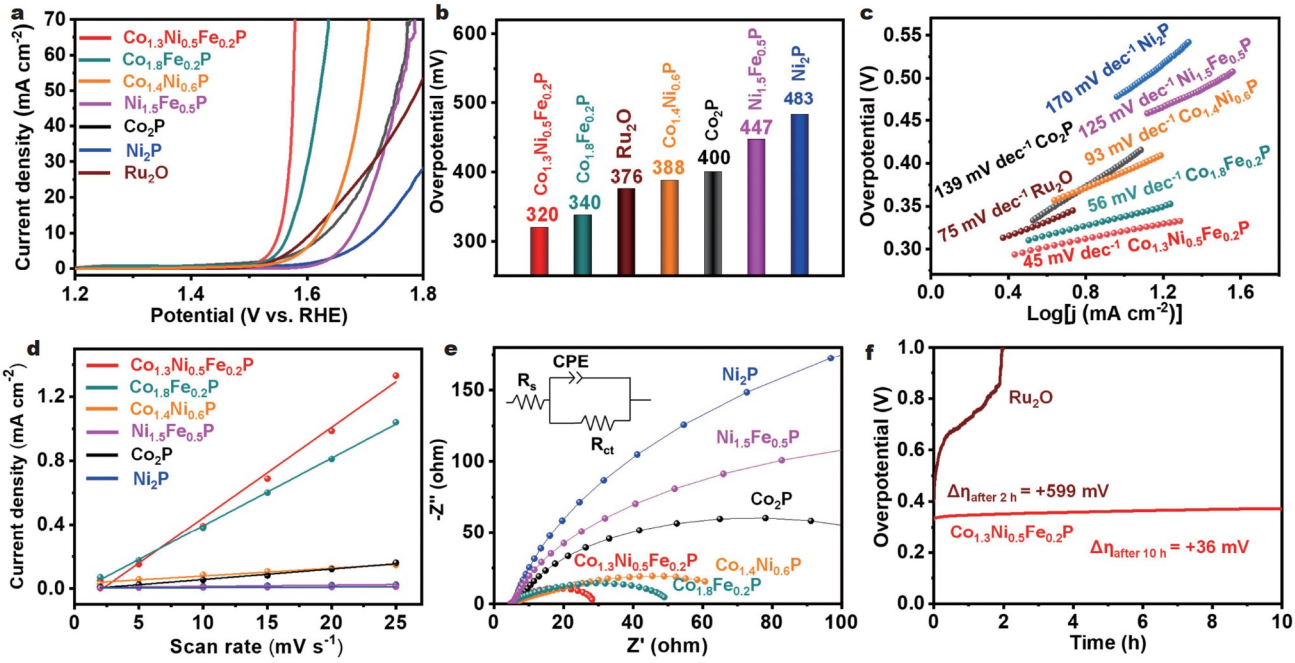

Figure 2 (a) LSV curves. (b) The overpotentials needed to deliver an anodic current density of 10 mA cm^{-2}. (c) Tafel slopes for $Co_{1.3}Ni_{0.5}Fe_{0.2}P$, $Co_{1.8}Fe_{0.2}P$, $Co_{1.4}Ni_{0.6}P$, $Ni_{1.5}Fe_{0.5}P$, Co_2P, Ni_2P, and commercial RuO_2. (d) Capacitive current density *versus* scan rate. (e) EIS Nyquist plots and analog circuit of $Co_{1.3}Ni_{0.5}Fe_{0.2}P$, $Co_{1.8}Fe_{0.2}P$, $Co_{1.4}Ni_{0.6}P$, $Ni_{1.5}Fe_{0.5}P$, Co_2P, and Ni_2P. (f) Chronopotentiometric curves on hierarchical $Co_{1.3}Ni_{0.5}Fe_{0.2}P$ and commercial Ru_2O catalyst with a constant current density of 10 mA cm^{-2}.

other samples, in accordance with the OER results. The low electrical impedance indicates that the electrical conductivity is improved by Ni/Fe substitution.

Moreover, stability is a key criterion to evaluate electrocatalysts for broader applications. Thus, the long-term stability of $Co_{1.3}Ni_{0.5}Fe_{0.2}P$ as an electrocatalyst was tested. As shown in Fig. 2f, for a constant current output at 10 mA cm^{-2}, $Co_{1.3}Ni_{0.5}Fe_{0.2}P$ shows an insignificant increment (36 mV) compared with the initial test after 10 h, while commercial RuO_2 displays a larger increment of 599 mV within 2 h.

Characterizations of electrocatalysts

As an optimization example, the scanning electron microscopy (SEM) images (Fig. S1c, d) exhibit that the as-prepared $Co_{1.3}Ni_{0.5}Fe_{0.2}(OH)_2$ possesses octahedral shapes with ultrathin nanosheet-constructed surface, which inherits the frames and sizes of the Cu_2O octahedron templates. The X-ray diffraction (XRD) characterization (Fig. S7) shows the amorphous structure of $Co_{1.3}Ni_{0.5}Fe_{0.2}(OH)_2$. Finally, $Co_{1.3}Ni_{0.5}Fe_{0.2}(OH)_2$ products are completely converted to $Co_{1.3}Ni_{0.5}Fe_{0.2}P$ *via* the phosphorization reaction. The SEM images of the as-prepared $Co_{1.3}Ni_{0.5}Fe_{0.2}P$ products (Fig. S1e, f) show that the phosphorization process maintains the octahedron structure and surface consistency. The transmission electron microscopy (TEM) images (Fig. 3a, b) show that the well-defined hierarchically hollow and porous structure with pleated nanosheet-constructed surface for $Co_{1.3}Ni_{0.5}Fe_{0.2}P$. In the high-resolution TEM (HRTEM) images (Fig. 3c, d) of hierarchical $Co_{1.3}Ni_{0.5}Fe_{0.2}P$, distinct lattice fringes with the *d*-spacings of about 0.193 and 0.219 nm could respectively correspond to the (211) and (110) planes of $Co_{1.3}Ni_{0.5}Fe_{0.2}P$, which is analogous to CoNiP (ICCD No. 71-2336) due to the very small amount of iron substitution [30]. Moreover, the selected area electron diffraction (SAED) pattern of hierarchical $Co_{1.3}Ni_{0.5}Fe_{0.2}P$ presenting a series of diffraction rings correspond to the (111), (200), (110), (211), and (210) crystalline planes of $Co_{1.3}Ni_{0.5}Fe_{0.2}P$ (Fig. 3e), revealing the polycrystalline nature of hierarchical $Co_{1.3}Ni_{0.5}Fe_{0.2}P$. The ultrathin nanosheet-constructed hollow nanostructure in hierarchical $Co_{1.3}Ni_{0.5}Fe_{0.2}P$ is clearly presented in the high-angle annular dark-field scanning TEM (HAADF-STEM) (Fig. 3f). The corresponding energy dispersive X-ray spectroscopy (EDX) element mapping images show the homogeneous distribution of Co, Ni, Fe, and P throughout hierarchical $Co_{1.3}Ni_{0.5}Fe_{0.2}P$ (Fig. 3g). Moreover, the EDX spectrum (Fig. S8) reveals that the atomic ratio of Co/Ni/Fe in hierarchical $Co_{1.3}Ni_{0.5}Fe_{0.2}P$ is close to 13:5:2. This data is also confirmed by ICP-AES and in good agreement with the Co/Ni/Fe atomic ratio in the initial reaction solution, indicating the successful composition control in the synthesis procedure.

The crystallinity and phase of the as-prepared samples with different atom ratios were characterized by XRD (Fig. S9). It is clear that unitary metal phosphides Co_2P and Ni_2P correspond well to Co_2P (ICCD No. 65-2380) and Ni_2P (ICCD No. 65-1989). While partial cobalt atoms in Co_2P were replaced by Ni atoms or Fe atoms and some Ni atoms in Ni_2P were replaced by Fe atoms, the main diffraction peak of (111) lattice plane of $Co_{1.4}Ni_{0.6}P$ exhibits a slight shift toward higher angles compared with the main diffraction peak of CoNiP (ICCD No. 71-2336), Co_2P (ICCD No. 65-2380), and Ni_2P (ICCD No. 65-1989), indicating that Ni atoms incorporated into the Co_2P crystalline lattice can alter the fringe lattice distance of the matrix phase due to the disparity in the radii of Co and Ni atoms [31].

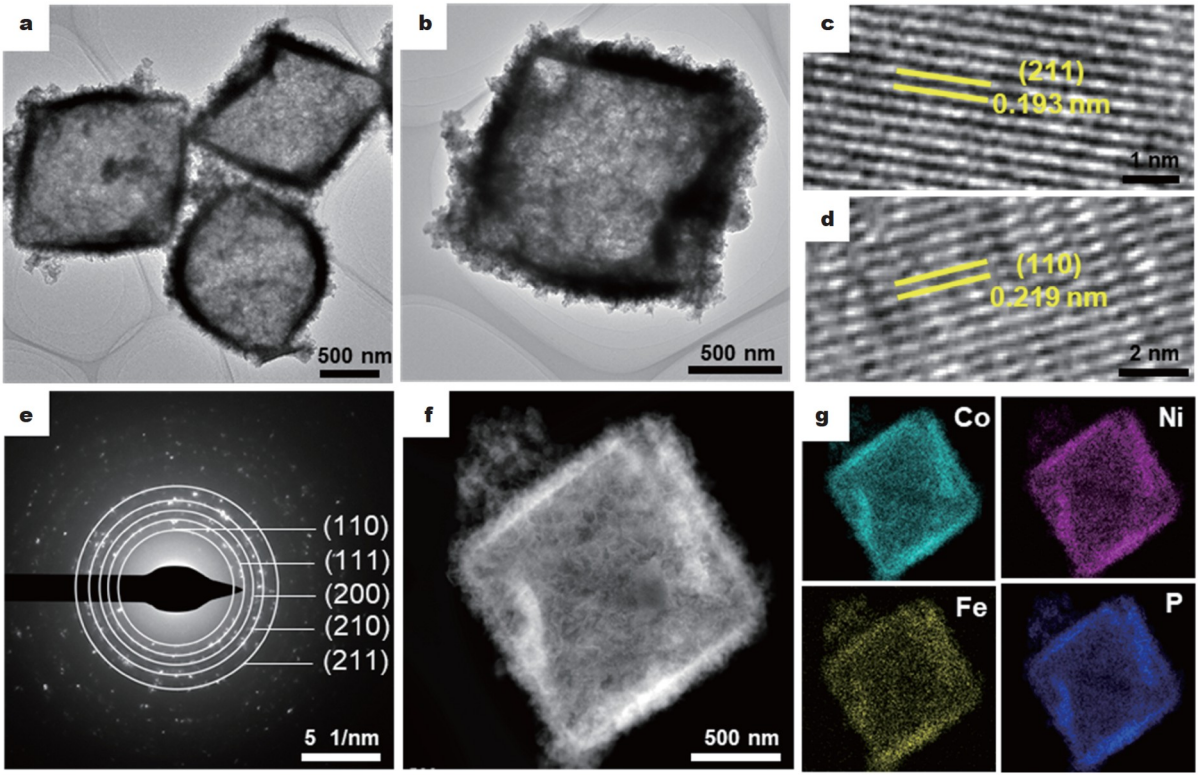

Figure 3 (a, b) TEM images, (c, d) HRTEM images, and (e) SAED pattern of hierarchical $Co_{1.3}Ni_{0.5}Fe_{0.2}P$. (f, g) HAADF-STEM image of hierarchical $Co_{1.3}Ni_{0.5}Fe_{0.2}P$ and its corresponding element mapping images of Co, Ni, Fe, and P.

When Fe was added to Co_2P or Ni_2P, the crystallinity of the product decreased seriously with only a very weak peak or no crystallization. For ternary metal phosphides $Co_{1.3}Ni_{0.5}Fe_{0.2}P$, due to the standard powder diffraction crystallographic data of CoNiFeP compounds are not available and the fact that Co/Ni is the parent metals, the diffraction peak of $Co_{1.3}Ni_{0.5}Fe_{0.2}P$ is similar to those of Co_2P (ICCD No. 65-2380), Ni_2P (ICCD No. 65-1989), and CoNiP (ICCD No. 71-2336), indicating complete phosphorization of the precursors. The XRD results of different trimetallic phosphides show that the crystallinity of the phosphides will decrease or even tend to be amorphous with the decrease of Ni content or the increase of Fe content (Fig. S10). Moreover, the main diffraction peaks of (111) lattice plane in $Co_{1.3}Ni_{0.5}Fe_{0.2}P$ are shifted to higher angle compared with Co_2P (ICCD No. 65-2380) and CoNiP (ICCD No. 71-2336) due to atomic replacement of Ni/Fe substitutions, and these results can show that new phases are generated rather than just the mixed phase [3]. In addition, N_2 adsorption-desorption measurement (Fig. S11a) shows that hierarchical $Co_{1.3}Ni_{0.5}Fe_{0.2}P$ possesses a specific surface area as high as 19.0 $m^2\ g^{-1}$, exceeding the previously reported transition metal compounds (Table S5). Benefiting from the advantage of the synthetic method using Cu_2O templates, hierarchical $Co_{1.3}Ni_{0.5}Fe_{0.2}P$ possesses a mesoporous structure (Fig. S11b), which could allow the reactants to enter the inner surface and improve the diffusion of reagents and exposure of active sites.

The survey spectrum of hierarchical $Co_{1.3}Ni_{0.5}Fe_{0.2}P$ in Fig. S12 shows the existence of Co, Ni, Fe, P, and O (oxygen may be from air). More precisely, the high-resolution Co 2p X-ray photoelectron spectroscopy (XPS) (Fig. 4a) shows that the two peaks located at 793.0 and 778.1 eV could be assigned to the Co $2p_{1/2}$ and Co $2p_{3/2}$ of Co species in Co-P because of a partial positive of Co metal [3]. The slight shifts of Co 2p suggest the partial positive charge ($Co^{\delta+}$) in metal phosphide (M-P). Besides, the peaks located at 797.5 and 781.6 eV are assigned to the Co $2p_{1/2}$ and Co $2p_{3/2}$ of the oxidized Co species, respectively, while the two corresponding peaks at 802.7 and 786.0 eV are related to the shakeup satellite peaks [32,33]. The high-resolution Ni 2p spectrum (Fig. 4b) exhibits three groups of peaks. The former two groups of peaks at 852.9/870.3 and 856.6/874.2 eV can be attributed to Ni-P and Ni-PO_x species, respectively. While the peaks at 861.8/880.0 eV are the satellite peaks [8,9,34]. Furthermore, two groups of spin-orbit doublets and one satellite peak of Fe 2p are shown in Fig. 4c, where the predominant peaks at 710.8 and 722.7 eV corresponded to Fe $2p_{3/2}$ and Fe $2p_{1/2}$, respectively, while the peaks at 713.5 and 726.9 eV could be ascribed to Fe^{3+}, and the main peak at 717.9 eV can be assigned to the satellite peak [35,36]. The XPS spectrum of P 2p shows three peaks assigned to phosphide at 129.0 and 129.6 eV, and phosphate or phosphide (PO_x or P-O species) at 133.7 eV (Fig. 4d) [37]. The formation of phosphate also enhances the OER activity because it can act as promoting ligand in the Co^{2+}/Co^{3+}/Co^{4+} redox process and facilitate the four-electron proton-coupled transfer steps during the OER [38]. In addition, more XPS measurements are carried out to evaluate the valence states and the surface composition of $Co_{1.3}Ni_{0.5}Fe_{0.2}P$, $Co_{1.4}Ni_{0.6}P$, $Co_{1.8}Fe_{0.2}P$, and Co_2P. It is noted that the peaks attributed to Co–P, Co–O, PO_x, and M–P bonds together were slightly shifted to lower binding energies for $Co_{1.8}Fe_{0.2}P$ and to higher binding energies for $Co_{1.4}Ni_{0.6}P$, as compared with those for the parent phosphide Co_2P (Fig. 4e, f). This result implies that the electron density redistribution occurs with the incorporation of Ni or Fe, leading to relatively negatively charged (with Fe incorporation) or positively charged (with Ni incorporation) element Co. With the simultaneous incorporation of Ni and Fe, similar charge shifts occur in $Co_{1.3}Ni_{0.5}Fe_{0.2}P$, indicating significant redistribution of electron densities for the Co atoms. Interestingly, compared with $Co_{1.4}Ni_{0.6}P$, the binding energies of Co–P, Co–O,

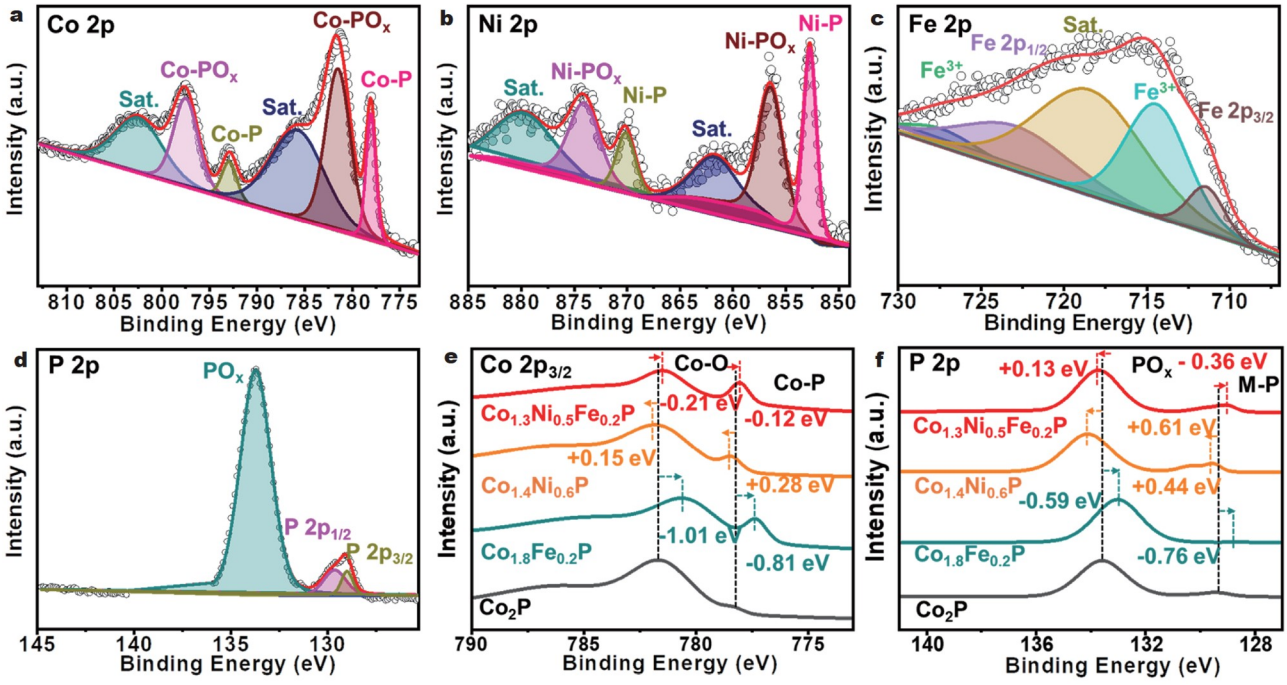

Figure 4 High-resolution XPS spectra for (a) Co 2p, (b) Ni 2p, (c) Fe 2p, and (d) P 2p of $Co_{1.3}Ni_{0.5}Fe_{0.2}P$. XPS survey spectra for (e) Co 2p and (f) P 2p of $Co_{1.3}Ni_{0.5}Fe_{0.2}P$, $Co_{1.8}Fe_{0.2}P$, $Co_{1.4}Ni_{0.6}P$, and Co_2P.

PO_x, M–P, and Ni–P bonds in $Co_{1.3}Ni_{0.5}Fe_{0.2}P$ decrease at the same time (Fig. S13a), while the binding energies of Ni–PO_x bonds increase. Similarly, compared with $Co_{1.8}Fe_{0.2}P$, the binding energies of Co–P, Co–O, PO_x, and M–P bonds in $Co_{1.3}Ni_{0.5}Fe_{0.2}P$ increase at the same time, while the binding energies of Fe^{3+} decrease (Fig. S13b). These results demonstrate that the simultaneous introduction of Ni and Fe could cause significant evolution in the electronic structures of the Co_2P, indicating strong electron interactions between Co, Ni, and Fe, which may have great significance in improving the catalytic reaction [17].

To further understand the chemical nature of the catalyst surface during the OER, XRD, SEM, XPS, and ICP characterizations of $Co_{1.3}Ni_{0.5}Fe_{0.2}P$ were conducted after a 10-h long-term stability test. The SEM image shows no morphological changes for $Co_{1.3}Ni_{0.5}Fe_{0.2}P$ after the prolonged electrocatalytic reaction (Fig. S14). XRD analysis shows that $Co_{1.3}Ni_{0.5}Fe_{0.2}P$ exhibits a clear change of the crystalline structure after the OER (Fig. S15). This suggests that the $Co_{1.3}Ni_{0.5}Fe_{0.2}P$ nanosheets are oxidized on the surface under the OER process, resulting in mostly metal oxides. Besides, the surface elemental change was further confirmed by the XPS analysis. In the high-resolution XPS spectra of Co 2p, Ni 2p, Fe 2p, and P 2p, all peaks associated with the metal phosphides completely disappear (Fig. S16). These observations suggest that CoNiFe oxides formed *in situ* are the catalytic OER active sites, which is consistent with the XRD results. The signal of P 2p after the 10-h stability test is very weak, resulting from the generation of M–O on the surface of the catalyst during the OER process, suggesting that the phosphates of the surface are etched [2,11,38]. Besides, the ICP-AES result also shows the leaching of phosphorus from $Co_{1.3}Ni_{0.5}Fe_{0.2}P$ surfaces (Table S6). Therefore, it can be deduced that during the OER in alkaline media, the surface of $Co_{1.3}Ni_{0.5}Fe_{0.2}P$ undergoes oxidation to polyphosphate and oxide containing species ($Co_{1.3}Ni_{0.5}Fe_{0.2}O_x$). Since the phosphates are highly soluble in alkaline solution, the surface becomes enriched with $Co_{1.3}Ni_{0.5}Fe_{0.2}O_x$, which is the true active electrocatalyst for the OER. According to the previous studies, M-based (M = Co, Ni, and Fe) materials are considered as pre-catalysts and then form the oxide/hydroxide catalysts in the OER process, and M–O is supposed as a highly active phase [36]. Moreover, the M-PO_x species accelerate water oxidation by proton-coupled electron transfer, which is beneficial to the catalytic process [39].

We further synthesized CoNiFe oxide using the same procedure for the synthesis of $Co_{1.3}Ni_{0.5}Fe_{0.2}P$ without adding the phosphorus source and compared the activity of the synthesized oxide with that of our synthesized phosphides. The metal ratio is also confirmed by ICP-AES (Table S7) and is in good agreement with the Co/Ni/Fe atomic ratio in the initial reaction solution, which reflects that our precise control strategy also applies to the synthesis of oxides. SEM image shows that it has a similar morphology with $Co_{1.3}Ni_{0.5}Fe_{0.2}P$ (Fig. S17), and the XRD pattern confirms that we successfully synthesized ternary metal oxides (Fig. S18), which is consistent with existing literature reports [40,41]. As expected, the activity of the corresponding oxide is very poor, much lower than that of $Co_{1.3}Ni_{0.5}Fe_{0.2}P$ (Fig. S19). This situation has also been reported in literature [42–44]. Hence, conventional synthesized transition metal oxides are quite different from the surface transition metal oxides formed during electrochemical measurement. By comparing the properties of metal phosphides and metal oxides, it is found that there is indeed a big difference in their electrochemical properties.

Theoretical calculations

Density function theory (DFT) calculations were further applied to uncover the fundamental mechanism of monometallic phosphides, bimetallic phosphides, and the obtained trimetallic phosphides on OER activity in our system. Hence, the crystal structures of $Co_{1.3}Ni_{0.5}Fe_{0.2}P$, $Co_{0.7}Ni_{0.7}Fe_{0.7}P$, $Co_{1.4}Ni_{0.6}P$, and Co_2P (Fig. 5a–d) are constructed to study the effect of Ni substitution and Ni-Fe co-substitution. Meanwhile, the calculated density of states (DOS) (Fig. 5a_1–d_1) of $Co_{1.3}Ni_{0.5}Fe_{0.2}P$, $Co_{0.7}Ni_{0.7}Fe_{0.7}P$, $Co_{1.4}Ni_{0.6}P$, and Co_2P catalysts reveal that the electronic structures of these catalysts are continuous near their Fermi levels, namely, their metallic characteristics [3,45–47]. With 30% of lattice Co atoms replaced by Ni in Co_2P (Fig. 5d_1), $Co_{1.4}Ni_{0.6}P$ (Fig. 5c_1) shows a slightly increased DOS for the occupied states around the Fermi level caused by the introduction of d-electrons of heteroatoms, which means that there has been only a minor improvement on the conductivity [48]. After Fe atoms further self-doped into $Co_{1.4}Ni_{0.6}P$, $Co_{1.3}Ni_{0.5}Fe_{0.2}P$ (Fig. 5b_1) has a clearly increased DOS near the Fermi level compared with $Co_{1.4}Ni_{0.6}P$. The high DOS of $Co_{1.3}Ni_{0.5}Fe_{0.2}P$ (Fig. 5a_1) indicates it could promote the charge transfer and facilitate the adsorption behaviors of intermediates on the metal centers, hence reducing the energy barriers for OER. When comparing $Co_{1.3}Ni_{0.5}Fe_{0.2}P$ and $Co_{0.7}Ni_{0.7}Fe_{0.7}P$, it can be clearly found that the DOS value of the former near the Fermi level is significantly greater than that of the latter, which further reflects the importance of precise regulation of atomic ratio. Besides, the DOS intensity near the Fermi level is related to electrical conductivity [49], which is consistent with the electron transfer resistance. As shown in Fig. 5a_2–d_2, the differential charge density distribution plots of $Co_{1.3}Ni_{0.5}Fe_{0.2}P$, $Co_{1.4}Ni_{0.6}P$, and Co_2P suggest the heteroatom doping intensifies the uneven distribution of charge. Interestingly, it is clear that the Bader charge values (−0.010, +0.228, and +0.213 eV) carried by the three cobalt atoms in the figures are consistent with the changes in the measured Co peaks of XPS. The Bader charge value of cobalt atom in $Co_{0.7}Ni_{0.7}Fe_{0.7}P$ (+0.061 eV) also shows a similar property lacking of electrons compared with $Co_{1.4}Ni_{0.6}P$ and Co_2P. Thus, the experimental and theoretical studies unveil that Ni-Fe co-substitution modulates the adsorption of OH^- on the $Co_{1.3}Ni_{0.5}Fe_{0.2}P$ surface to be more thermo-neutral, thus improving the OER catalytic performance.

In view of the leaching of the phosphorus element and the metal atoms oxidized, the models of $Co_{1.3}Ni_{0.5}Fe_{0.2}P$, $Co_{0.7}Ni_{0.7}Fe_{0.7}P$, $Co_{1.4}Ni_{0.6}P$, and Co_2P are re-constructed by replacing P atoms with O atoms completely. To some extent, this reflects the change of surface structure in the initial stage. Based on the above consideration, the crystal structures of $Co_{1.3}Ni_{0.5}Fe_{0.2}O$, $Co_{0.7}Ni_{0.7}Fe_{0.7}O$, $Co_{1.4}Ni_{0.6}O$, and Co_2O are constructed to study the effect of Ni substitution and Ni-Fe co-substitution (Fig. 5e–h). The calculated DOSs of $Co_{1.3}Ni_{0.5}Fe_{0.2}O$, $Co_{0.7}Ni_{0.7}Fe_{0.7}O$, $Co_{1.4}Ni_{0.6}O$, and Co_2O catalysts reveal their metallic characteristics just like their corresponding phosphides (Fig. 5e_1–h_1). Along with 30% of lattice Co atoms replaced by Ni in Co_2O, $Co_{1.4}Ni_{0.6}O$ shows a great improvement in DOS for the occupied states around the Fermi level caused by the introduction of d-electrons of heteroatoms, which means that there has been a clear enhancement on the conductivity [48]. After Fe

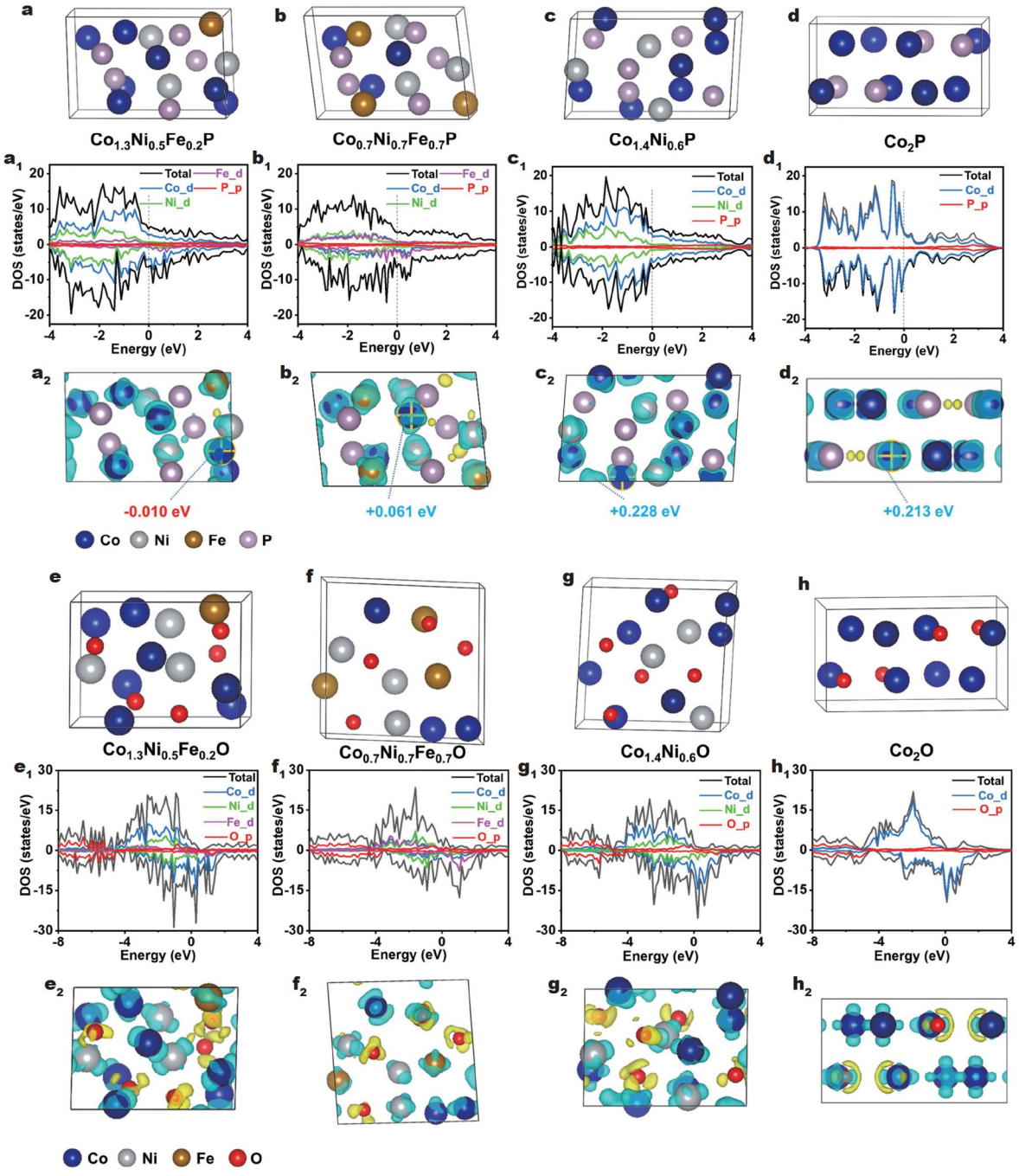

Figure 5 (a–d) Structure representation of (a) $Co_{1.3}Ni_{0.5}Fe_{0.2}P$, (b) $Co_{0.7}Ni_{0.7}Fe_{0.7}P$, (c) $Co_{1.4}Ni_{0.6}P$, and (d) Co_2P unit cell; (a_1–d_1) calculated density of states and (a_2–d_2) the charge density differences (yellow region indicates charge accumulation; cyan region indicates charge depletion; the numbers are bader charge values) corresponding to (a–d). (e–h) Structure representation of (e) $Co_{1.3}Ni_{0.5}Fe_{0.2}O$, (f) $Co_{0.7}Ni_{0.7}Fe_{0.7}O$, (g) $Co_{1.4}Ni_{0.6}O$, and (h) Co_2O unit cell. (e_1–h_1) Calculated density of states and (e_2–h_2) charge density differences (yellow region indicates charge accumulation; cyan region indicates charge depletion) corresponding to (e–h).

atoms further self-doped into $Co_{1.4}Ni_{0.6}O$, $Co_{1.3}Ni_{0.5}Fe_{0.2}O$ has a clearly increased DOS near the Fermi level compared with $Co_{1.4}Ni_{0.6}O$. The high DOS of $Co_{1.3}Ni_{0.5}Fe_{0.2}O$ indicates it could accelerate the charge transfer and facilitate the adsorption behaviors of intermediates on the Co/Ni/Fe atom centers, hence reducing the energy barriers for OER. When comparing $Co_{1.3}Ni_{0.5}Fe_{0.2}O$ and $Co_{0.7}Ni_{0.7}Fe_{0.7}O$, it can be clearly found that the DOS value of the former near the Fermi level is significantly greater than that of the latter, which further demonstrates the importance of precise regulation of atomic ratio. Besides, the differential charge density distribution plots of $Co_{1.3}Ni_{0.5}Fe_{0.2}O$, $Co_{0.7}Ni_{0.7}Fe_{0.7}O$, $Co_{1.4}Ni_{0.6}O$, and Co_2O suggest the heteroatom doping changes the charge distribution (Fig. 5e_2–h_2). The asymmetric atomic $Co_{1.3}Ni_{0.5}Fe_{0.2}O$ site undergoes a strongly symmetry-breaking charge transfer, leading to charge polarization and electron redistribution compared with other three

models, which may promote the OER process [50,51].

CONCLUSIONS

We have presented an effective strategy to synthesize hierarchical CoNiFeP with precise control of stoichiometric metallic elements. The influence of different molar ratios of Co/Ni/Fe on the electronic structures and electrocatalytic properties of trimetallic phosphides has been fully investigated. Hierarchical $Co_{1.3}Ni_{0.5}Fe_{0.2}P$ with the optimal composition represents much improved electrocatalytic activity for OER as compared with monometallic phosphides, bimetallic phosphides, and other obtained trimetallic phosphides, even superior to the noble metal-based catalyst. It is found that the surface of $Co_{1.3}Ni_{0.5}Fe_{0.2}P$ underwent oxidation during the OER process. DFT calculations of samples before and after long-term stability tests reveal the important role of metal composition in modulating the activity of transition-metal-based catalysts, and provide scientific guidance for the design of high-performance OER catalysts in alkaline media. The high performance of hierarchical $Co_{1.3}Ni_{0.5}Fe_{0.2}P/Co_{1.3}Ni_{0.5}Fe_{0.2}O$ is ascribed to the modulation of the adsorption of OH^-, rapid charge transfer kinetics, and optimized M–P/M–O binding energy. The proposed synthesis method could provide an important reference for the preparation of multi-metallic phosphides with precise adjustment of stoichiometric compositions.

Received 28 January 2022; accepted 1 April 2022; published online 25 May 2022

1 Wu R, Xiao B, Gao Q, *et al.* A Janus nickel cobalt phosphide catalyst for high-efficiency neutral-pH water splitting. Angew Chem Int Ed, 2018, 57: 15445–15449
2 Lian Y, Sun H, Wang X, *et al.* Carved nanoframes of cobalt-iron bimetal phosphide as a bifunctional electrocatalyst for efficient overall water splitting. Chem Sci, 2019, 10: 464–474
3 Qiu B, Cai L, Wang Y, *et al.* Fabrication of nickel-cobalt bimetal phosphide nanocages for enhanced oxygen evolution catalysis. Adv Funct Mater, 2018, 28: 1706008
4 Xiao X, He CT, Zhao S, *et al.* A general approach to cobalt-based homobimetallic phosphide ultrathin nanosheets for highly efficient oxygen evolution in alkaline media. Energy Environ Sci, 2017, 10: 893–899
5 Septiani NLW, Kaneti YV, Fathoni KB, *et al.* Self-assembly of two-dimensional bimetallic nickel-cobalt phosphate nanoplates into one-dimensional porous chainlike architecture for efficient oxygen evolution reaction. Chem Mater, 2020, 32: 7005–7018
6 Xiao YX, Ying J, Tian G, *et al.* Highly dispersed PtPd on graphitic nanofibers and its heavy d-π effect. Appl Catal B-Environ, 2019, 259: 118080
7 Xiao YX, Ying J, Tian G, *et al.* PtPd hollow nanocubes with enhanced alloy effect and active facets for efficient methanol oxidation reaction. Chem Commun, 2021, 57: 986–989
8 Wang XD, Chen HY, Xu YF, *et al.* Self-supported $NiMoP_2$ nanowires on carbon cloth as an efficient and durable electrocatalyst for overall water splitting. J Mater Chem A, 2017, 5: 7191–7199
9 Lv X, Li X, Yang C, *et al.* Large-size, porous, ultrathin NiCoP nanosheets for efficient electro/photocatalytic water splitting. Adv Funct Mater, 2020, 30: 1910830
10 Yan L, Cao L, Dai P, *et al.* Metal-organic frameworks derived nanotube of nickel-cobalt bimetal phosphides as highly efficient electrocatalysts for overall water splitting. Adv Funct Mater, 2017, 27: 1703455
11 Li D, Baydoun H, Verani CN, *et al.* Efficient water oxidation using CoMnP nanoparticles. J Am Chem Soc, 2016, 138: 4006–4009
12 Xu J, Li J, Xiong D, *et al.* Trends in activity for the oxygen evolution reaction on transition metal (M = Fe, Co, Ni) phosphide pre-catalysts. Chem Sci, 2018, 9: 3470–3476
13 Suen NT, Hung SF, Quan Q, *et al.* Electrocatalysis for the oxygen evolution reaction: Recent development and future perspectives. Chem Soc Rev, 2017, 46: 337–365
14 Sun Y, Sun S, Yang H, *et al.* Spin-related electron transfer and orbital interactions in oxygen electrocatalysis. Adv Mater, 2020, 32: 2003297
15 Zhang G, Wang G, Liu Y, *et al.* Highly active and stable catalysts of phytic acid-derivative transition metal phosphides for full water splitting. J Am Chem Soc, 2016, 138: 14686–14693
16 Kepp KP. A quantitative scale of oxophilicity and thiophilicity. Inorg Chem, 2016, 55: 9461–9470
17 Wang M, Dong CL, Huang YC, *et al.* Electronic structure evolution in tricomponent metal phosphides with reduced activation energy for efficient electrocatalytic oxygen evolution. Small, 2018, 14: 1801756
18 He B, Xu C, Tang Y, *et al.* Facile fabrication of a hierarchical NiCoFeP hollow nanoprism for efficient oxygen evolution in the Zn–air battery. J Mater Chem A, 2019, 7: 24964–24972
19 Tan Y, Wang H, Liu P, *et al.* Versatile nanoporous bimetallic phosphides towards electrochemical water splitting. Energy Environ Sci, 2016, 9: 2257–2261
20 Feng H, Tang L, Zeng G, *et al.* Electron density modulation of $Fe_{1-x}Co_xP$ nanosheet arrays by iron incorporation for highly efficient water splitting. Nano Energy, 2020, 67: 104174
21 Li S, Wang X, Li M, *et al.* Self-supported ternary $(Ni_xFe_y)_2P$ nanoplates arrays as an efficient bifunctional electrocatalyst for overall water splitting. Electrochim Acta, 2019, 319: 561–568
22 Shannon RD. Revised effective ionic radii and systematic studies of interatomic distances in halides and chalcogenides. Acta Cryst A, 1976, 32: 751–767
23 Dean JA (eds.). Lange's Handbook of Chemistry. New York: McGraw-Hill, 2004
24 Wang Y, Jiang K, Zhang H, *et al.* Bio-inspired leaf-mimicking nanosheet/nanotube heterostructure as a highly efficient oxygen evolution catalyst. Adv Sci, 2015, 2: 1500003
25 Zhang R, Wang X, Yu S, *et al.* Ternary $NiCo_2P_x$ nanowires as pH-universal electrocatalysts for highly efficient hydrogen evolution reaction. Adv Mater, 2017, 29: 1605502
26 Yan D, Li Y, Huo J, *et al.* Defect chemistry of nonprecious-metal electrocatalysts for oxygen reactions. Adv Mater, 2017, 29: 1606459
27 Wang Y, Yu HZ, Ying J, *et al.* Ultimate corrosion to Pt-Cu electrocatalysts for enhancing methanol oxidation activity and stability in acidic media. Chem Eur J, 2021, 27: 9124–9128
28 Ying J, Jiang G, Paul Cano Z, *et al.* Nitrogen-doped hollow porous carbon polyhedrons embedded with highly dispersed Pt nanoparticles as a highly efficient and stable hydrogen evolution electrocatalyst. Nano Energy, 2017, 40: 88–94
29 Dong Y, Ying J, Xiao YX, *et al.* Highly dispersed Pt nanoparticles embedded in N-doped porous carbon for efficient hydrogen evolution. Chem Asian J, 2021, 16: 1878–1881
30 Li W, Gao X, Wang X, *et al.* From water reduction to oxidation: Janus Co-Ni-P nanowires as high-efficiency and ultrastable electrocatalysts for over 3000 h water splitting. J Power Sources, 2016, 330: 156–166
31 Liang H, Gandi AN, Anjum DH, *et al.* Plasma-assisted synthesis of NiCoP for efficient overall water splitting. Nano Lett, 2016, 16: 7718–7725
32 Xia C, Jiang Q, Zhao C, *et al.* Selenide-based electrocatalysts and scaffolds for water oxidation applications. Adv Mater, 2016, 28: 77–85
33 Li Y, Liu J, Chen C, *et al.* Preparation of NiCoP hollow quasi-polyhedra and their electrocatalytic properties for hydrogen evolution in alkaline solution. ACS Appl Mater Interfaces, 2017, 9: 5982–5991
34 Wang L, Fan J, Liu Y, *et al.* Phase-modulation of iron/nickel phosphides nanocrystals "armored" with porous P-doped carbon and anchored on P-doped graphene nanohybrids for enhanced overall water splitting. Adv Funct Mater, 2021, 31: 2010912
35 Liu G, Zhao Y, Yao R, *et al.* Realizing high performance solar water oxidation for Ti-doped hematite nanoarrays by synergistic decoration with ultrathin cobalt-iron phosphate nanolayers. Chem Eng J, 2019, 355: 49–57
36 Zhan K, Feng C, Feng X, *et al.* Iron-doped nickel cobalt phosphide nanoarrays with urchin-like structures as high-performance electro-

catalysts for oxygen evolution reaction. ACS Sustain Chem Eng, 2020, 8: 6273–6281
37 Qin Q, Jang H, Li P, *et al.* A tannic acid-derived N-, P-codoped carbon-supported iron-based nanocomposite as an advanced trifunctional electrocatalyst for the overall water splitting cells and zinc-air batteries. Adv Energy Mater, 2019, 9: 1803312
38 Beltrán-Suito R, Menezes PW, Driess M. Amorphous outperforms crystalline nanomaterials: surface modifications of molecularly derived CoP electro(pre)catalysts for efficient water-splitting. J Mater Chem A, 2019, 7: 15749–15756
39 Yan L, Zhang B, Wu S, *et al.* A general approach to the synthesis of transition metal phosphide nanoarrays on MXene nanosheets for pH-universal hydrogen evolution and alkaline overall water splitting. J Mater Chem A, 2020, 8: 14234–14242
40 Xu Y, Özcan F, Zielke P, *et al.* Continuous hydrothermal flow synthesis of $Co_{1-x}Ni_xFe_2O_4$ (x = 0–0.8) nanoparticles and their catalytic properties for CO oxidation and oxygen evolution reaction. Z Anorg Allg Chem, 2018, 644: 1727–1733
41 Xiang J, Chu Y, Shen X, *et al.* Electrospinning preparation, characterization and magnetic properties of cobalt-nickel ferrite ($Co_{1-x}Ni_xFe_2O_4$) nanofibers. J Colloid Interface Sci, 2012, 376: 57–61
42 Stern LA, Feng L, Song F, *et al.* Ni_2P as a Janus catalyst for water splitting: The oxygen evolution activity of Ni_2P nanoparticles. Energy Environ Sci, 2015, 8: 2347–2351
43 Dutta A, Samantara AK, Dutta SK, *et al.* Surface-oxidized dicobalt phosphide nanoneedles as a nonprecious, durable, and efficient OER catalyst. ACS Energy Lett, 2016, 1: 169–174
44 Mabayoje O, Shoola A, Wygant BR, *et al.* The role of anions in metal chalcogenide oxygen evolution catalysis: Electrodeposited thin films of nickel sulfide as "pre-catalysts". ACS Energy Lett, 2016, 1: 195–201
45 Xiao YX, Ying J, Chen JB, *et al.* Confined ultrafine Pt in porous carbon fibers and their N-enhanced heavy d-π effect. Chem Mater, 2022, 34: 3705–3714
46 Asnavandi M, Yin Y, Li Y, *et al.* Promoting oxygen evolution reactions through introduction of oxygen vacancies to benchmark NiFe–OOH catalysts. ACS Energy Lett, 2018, 3: 1515–1520
47 Zhou Y, Sun S, Song J, *et al.* Enlarged Co–O covalency in octahedral sites leading to highly efficient spinel oxides for oxygen evolution reaction. Adv Mater, 2018, 30: 1802912
48 Zhao Y, Wan W, Chen Y, *et al.* Understanding and optimizing ultrathin coordination polymer derivatives with high oxygen evolution performance. Adv Energy Mater, 2020, 10: 2002228
49 Liu C, Zhang G, Yu L, *et al.* Oxygen doping to optimize atomic hydrogen binding energy on NiCoP for highly efficient hydrogen evolution. Small, 2018, 14: 1800421
50 Xiao YX, Ying J, Tian G, *et al.* Hierarchically fractal PtPdCu sponges and their directed mass- and electron-transfer effects. Nano Lett, 2021, 21: 7870–7878
51 Xiao M, Zhu J, Li S, *et al.* 3d-Orbital occupancy regulated Ir-Co atomic pair toward superior bifunctional oxygen electrocatalysis. ACS Catal, 2021, 11: 8837–8846

Acknowledgements This work was financially supported by the National Natural Science Foundation of China (51861135313), Sino-German Center COVID-19 Related Bilateral Collaborative project (C-0046), FRFCU (2021qntd13), the National 111 project (B20002), Guangdong Basic and Applied Basic Research Foundation (2019A1515110436, 2021A1515111131, and 2022A1515011905), Guangdong Province International Scientific and Technological Cooperation Projects (2020A0505100036), Guangzhou Science and Technology Project (202102020463), Shenzhen Science and Technology Program (JCYJ20210324142010029), and DSI/NRF/WITS South African Research Chair Initiative (SARChI) Chair (132739).

Author contributions Ying J and Yang X conceived and supervised this study; Chen J carried out the materials fabrication, characterizations, electrochemical measurements, DFT calculations, and computational models; Xiao Y and Dong Y assisted in drawing the pictures. Chen J wrote the paper; Ying J, Yang X, Ozoemena KI, and Lenaerts S revised the paper. All authors discussed the results and commented on the manuscript.

Conflict of interest The authors declare that they have no conflict of interest.

Supplementary information Experimental details and supporting data are available in the online version of the paper.

Jiangbo Chen received his Bachelor degree in materials chemistry at Wuhan Textile University in 2018. He is currently a PhD candidate under the supervision of Prof. Xiaoyu Yang at Wuhan University of Technology. His research interest focuses on non-noble metal compounds in the electrocatalysis field.

Jie Ying received his PhD degree from Wuhan University of Technology in 2016. He then joined the University of Waterloo and Heinrich-Heine-Universität Düsseldorf as a postdoctoral fellow. Currently, he is an associate professor at Sun Yat-sen University. His scientific interest includes the design and synthesis of nanocomposites and their application in catalysis and electrocatalysis.

Xiaoyu Yang earned his BS degree from Jilin University in 2000 and his joint PhD degree from Jilin University, China and FUNDP, Belgium (co-education) in 2007. After a postdoctoral fellowship at the FUNDP, he worked as a "Chargé de Recherches" at the F.N.R.S. of Belgium. He is currently working as a full professor at the State Key Laboratory of Advanced Technology for Material Synthesis and Processing and a visiting professor at Harvard University.

分级FeCoNi磷化物的计量设计及其高效析氧性能

陈江波[1], 应杰[2*], 肖宇轩[2], 董缘[1], Kenneth I. Ozoemena[3], Silvia Lenaerts[4], 阳晓宇[1,5*]

摘要 过渡金属磷化物是电催化设计中的新兴材料, 而多元金属磷化物因其能显著提高电催化活性而备受关注. 然而, 由于不同种类金属前驱物之间水解和缩合速率的差异, 当前有关超过两种金属元素和化学计量比精确控制的多元金属磷化物的报道非常少. 因此, 合理设计多元金属磷化物的组成对提高其催化性能具有重要意义. 本工作通过直接磷化二价过渡金属离子氢氧化物的合成策略, 制备了能够精确控制化学计量比(x:y:z = (1–10):(1–10):1)的分级结构$Co_xNi_yFe_zP$, 其中具有最优组分的$Co_{1.3}Ni_{0.5}Fe_{0.2}P$在析氧反应(OER)中展示了优异的催化活性和高稳定性. 密度泛函理论计算表明, 相对于其他组分的过渡金属磷化物, $Co_{1.3}Ni_{0.5}Fe_{0.2}P$在费米能级附近的态密度明显增加, 这可以增强催化剂对OH^-的吸附, 从而提升OER性能.

